W. C. Tang, T.-C. H. Nguyen, and R. T. Howe, "Laterally driven polysilicon resonant microstructures," *Sensors and Actuators,* **20**, 25-32, 1989.

Sensors and Actuators, *20* (1989) 25–32

Laterally Driven Polysilicon Resonant Microstructures

WILLIAM C. TANG, TU-CUONG H. NGUYEN and ROGER T. HOWE

Berkeley Sensor and Actuator Center, Department of Electrical Engineering and Computer Sciences and the Electronics Research Laboratory, University of California, Berkeley, CA 94720 (U.S.A.)

Abstract

Interdigitated finger (comb) structures are demonstrated to be effective for exciting electrostatically the resonance of polysilicon microstructures parallel to the plane of the substrate. Linear plates suspended by a folded-cantilever truss and torsional plates suspended by spiral and serpentine springs are fabricated from a 2 μm-thick phosphorus-doped low-pressure chemical-vapor-deposited (LPCVD) polysilicon film. Resonance is observed visually, with frequencies ranging from 18 kHz to 80 kHz and quality factors from 20 to 130. Simple beam theory is adequate for calculating the resonance frequencies, using a Young's modulus of 140 GPa and neglecting residual strain in the released structures.

1. Introduction

Resonant micromechanical structures are used as transducing elements in a wide variety of sensors. These devices utilize the high sensitivity of the frequency of a mechanical resonator to physical or chemical parameters that affect its potential or kinetic vibrational energy [1–4]. Microfabricated resonant structures for sensing pressure [5–7], acceleration [8] and vapor concentration [9] have been demonstrated.

Mechanical vibration of microstructures can be excited in several ways, including piezoelectric films [5], thermal expansion [8, 10], electrostatic forces [1, 6, 11, 12] and magnetostatic forces [7]. Vibration can be detected by means of piezoelectric films [5], piezoresistive strain gauges [10], optical techniques [10, 12, 13] and capacitively [1, 6, 9, 11]. Electrostatic excitation combined with capacitive (electrostatic) detection is an attractive approach for silicon microstructures because of the simplicity and compatibility with micromachining technology [1, 2].

Both crystalline silicon [6] and polycrystalline silicon (polysilicon) [9] microstructures have been driven and sensed electrostatically by means of fixed electrodes forming parallel-plate capacitors with the structure. However, there are several drawbacks to the parallel-plate-capacitor driving and sensing of micromechanical structures. The electrostatic force is non-linear unless the amplitude of vibration is limited to a small fraction of the capacitor gap. In addition, the quality factor Q of the resonance is very low at atmospheric pressure because of squeeze-film damping in the micron-sized capacitor gap [9]. If the microstructure is resonated in vacuum, the efficient parallel-plate excitation and the very high intrinsic Q lead to steady-state excitation voltages with mV-level amplitudes. Such low voltage levels complicate the design of the sustaining amplifier [14].

In this paper, we describe the design, fabrication and initial testing of an electrostatic comb structure for exciting and sensing the vibration of polysilicon microstructures *parallel* to the plane of the substrate. Interdigitated fingers and the mechanical structure are etched in a single LPCVD polysilicon film, which has been deposited on a patterned sacrificial oxide layer. The drive capacitance is linear with displacement of the structure, resulting in a force that is independent of the vibration amplitude. Moreover, the vibration amplitude can be of the order of 10 μm for certain comb and structure designs. The use of weaker fringing fields to excite resonance is advantageous for high-Q structures (resonating in vacuum), since this results in larger steady-state excitation voltages. Furthermore, the quality factor for lateral vibration at atmospheric pressure is substantially higher than for vibration normal to the substrate [15, 16]. Couette flow in the gap between the structure and the substrate occurs for lateral motion of the structure, which is much less dissipative than squeeze-film damping [15]. Another significant advantage of the lateral-drive concept is that a variety of elaborate geometric structures, such as differential capacitive excitation and detection, can be incorporated without an increase in process complexity. This flexibility is being exploited in current efforts to develop a microactuator technology based on lateral resonant structures [17].

Elsevier Sequoia/Printed in The Netherlands

The theory of the electrostatic comb drive is derived first and used to obtain electromechanical transfer functions for generalized lateral structures. We next present the design and modeling of a linear resonant structure with a truss suspension and a torsional resonant structure using a spiral-spring suspension or a serpentine-spring suspension. The fabrication process, a straightforward application of surface micromachining technology, is then described. Initial measurements of resonance frequencies and quality factors are compared with analytical and finite-element calculations.

2. Electrostatic Comb Drive

Figure 1 shows the layout of a linear resonant structure that can be driven electrostatically from one side and sensed capacitively at the other side with interdigitated finger (comb) structures. Alternatively, the structure can be driven differentially (push–pull) using the two combs, with the motion sensed by the impedance shift at resonance [14]. In analyzing the electromechanical transfer function, we consider the former, two-port configuration. The motion is sensed by detecting the short-circuit current through the time-varying interdigitated capacitor with a d.c. bias [1].

The driving force and the output sensitivity are both proportional to the variation of the comb capacitance C with the lateral displacement x of the structure. A key feature of the electrostatic-comb drive is that $\partial C/\partial x$ is a constant, independent of the displacement x, as long as x is less than the finger overlap (Fig. 1). Therefore, electrostatic comb drives can have linear electromechanical transfer functions for large displacements, in contrast to parallel-plate capacitive drives.

At the sense port, harmonic motion of the structure in Fig. 1 results in a sense current, i_s, which is given by

$$i_s = V_S(\partial C/\partial x)(\partial x/\partial t) \tag{1}$$

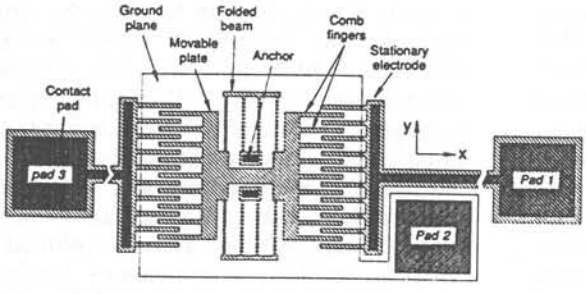

Fig. 1. Layout of a linear resonant plate.

where V_S is the bias voltage between the structure and the stationary sense electrode. At the drive port, the static displacement x as a function of drive voltage is given by

$$x = \frac{F_x}{k_{sys}} = \frac{v_D^2(\partial C/\partial x)}{2k_{sys}} \tag{2}$$

where F_x is the electrostatic force in the x-direction, k_{sys} is the system spring constant and v_D is the drive voltage.

For a drive voltage $v_D(t) = V_P + v_d \sin(\omega t)$, where V_P is the d.c. bias and v_d is the a.c. drive amplitude, the time derivative of x is

$$\frac{\partial x}{\partial t} = \frac{(\partial C/\partial x)}{2k_{sys}} \frac{\partial (v_D^2)}{\partial t} = \frac{(\partial C/\partial x)}{2k_{sys}} [2\omega V_P v_d \cos(\omega t) + \omega v_d^2 \sin(2\omega t)] \tag{3}$$

where we have used the fact that $(\partial C/\partial x)$ is a constant for the interdigitated-finger capacitor. The second-harmonic term on the right-hand side of eqn. (3) is negligible if $v_d \ll V_P$. Furthermore, if a push–pull drive is used, this term results in a common-mode force and is cancelled to first order. At mechanical resonance, the magnitude of the linear term in eqn. (3) is multiplied by the quality factor Q [1, 9], from which it follows that the magnitude of the transfer function $T(j\omega_r) = X/V_d$ relating the phasor displacement X to phasor drive voltage V_d at the resonance frequency ω_r is:

$$\left|\frac{X}{V_d}\right| = V_P \frac{Q}{k_{sys}} (\partial C/\partial x) \tag{4}$$

The transconductance of the resonant structure is defined by $G(j\omega) = I_s/V_d$. Its magnitude at resonance can be found by substitution of eqn. (4) into the phasor form of eqn. (1):

$$\left|\frac{I_s}{V_d}\right| = \omega V_P V_S \frac{Q}{k_{sys}} (\partial C/\partial x)^2 \tag{5}$$

A planar electrode extends under the comb and the plate in Fig. 1, which can be grounded or set to a d.c. potential in order to minimize parasitic capacitive coupling between the drive and sense ports. An additional function of this electrode is to suppress the excitation of undesired modes of the structure.

3. Resonant Structure Design

We now consider the mechanical design of two classes of lateral resonant structures, which demonstrate the power and flexibility of the lateral drive approach: linear resonant plates with folded supporting beams and torsional resonant plates with differential drive and sense ports.

3.1. Linear Resonant Plates

Figure 1 shows the layout of a linear resonant plate with a 50 μm-long folded-beam suspension. Motivations for this truss suspension are its large compliance and its capability for relief of built-in residual strain in the structural film. The folded cantilever beams are anchored near the center, thus allowing expansion or contraction of the four beams to take place along the y-axis (Fig. 1). Both the average residual stress in the polysilicon film and stress induced by large-amplitude plate motion should be largely relieved by this design. In addition, the long effective support lengths result in a highly compliant suspension. Plates with 200 μm-long trusses are resonated with amplitudes as large as 10 μm.

An accurate analytical expression for the fundamental lateral resonance frequency, f_r, can be found using Rayleigh's method:

$$f_r = \frac{1}{2\pi}\left[\frac{k_{sys}}{(M_p + 0.3714M)}\right]^{1/2} \tag{6}$$

where M_p and M are the masses of the plate and of the supporting beams, respectively. For the folded-beam structure, an analytical expression for k_{sys} can be found by assuming that the trusses joining the folded-beam segments are rigid:

$$k_{sys} = 24EI/L^3 = 2Eh(W/L)^3 \tag{7}$$

where $I = hW^3/12$ is the moment of inertia of the beams, with h, W and L being the thickness, width, and length of each beam, respectively. Residual strain in the structure is neglected in finding this expression. Combining eqns. (6) and (7), it follows that

$$f_r = \frac{1}{2\pi}\left[\frac{2Eh(W/L)^3}{(M_p + 0.3714M)}\right]^{1/2} \tag{8}$$

The quality factor Q is estimated by assuming that Couette flow underneath the plate is the dominant dissipative process [16]:

$$Q = \frac{d}{\mu A_p}(Mk_{sys})^{1/2} \tag{9}$$

where μ is the absolute viscosity of air (1.8×10^{-5} N s m^{-2}), A_p is the surface area of the plate, and d is the offset between the plate and the substrate. Quality factors for lateral motion are much higher than for motion normal to the substrate [9, 18].

3.2. Torsional Resonant Plates

Another class of structures is driven into torsional resonance by a set of concentric interdigitated electrodes. Figure 2 shows one of the designs with two Archimedean spirals as supporting beams. Figure 3 is a scanning-electron micrograph (SEM) of another design using four serpentine springs. The structures are supported only at the center, enabling the built-in residual stress in the polysilicon film to relax somewhat. An advantage of the torsional approach is that four or more pairs of balanced concentric comb structures can be placed at the perimeter of the ring, providing for high degree of flexibility for differential drive and sense. Since both the drive and the sense ports are differentially balanced, excitation of undesired oscillation modes is avoided and signal corruption by feedthrough is minimized. As with the lateral structure, extensive ground planes are utilized.

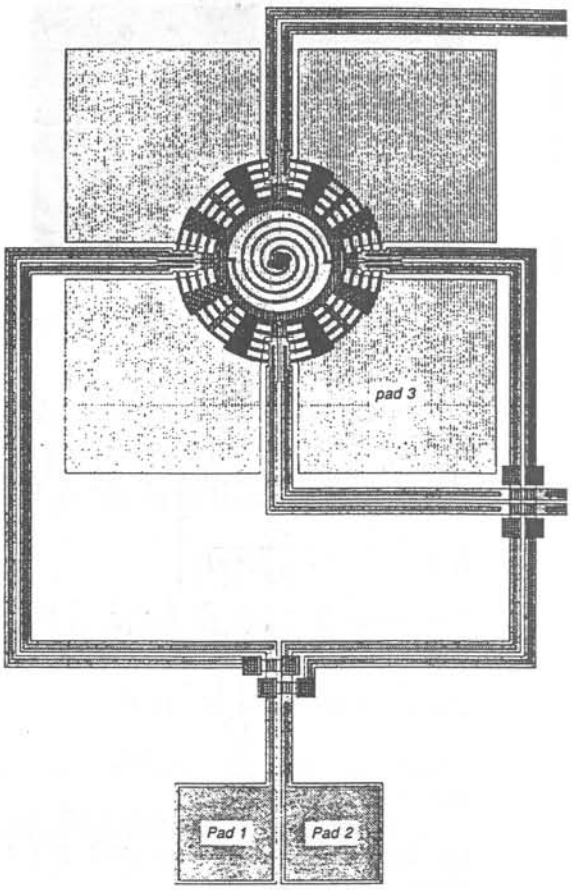

Fig. 2. Layout of a torsional resonant plate supported by two Archimedean spirals.

The torsional spring constant of the Archimedean spiral is given by [19]:

$$k_\theta = \frac{EhW^3}{12L}(\mu\text{N}\,\mu\text{m rad}^{-1}) \tag{10}$$

where L is the length of the spiral. As was done for the lateral resonant structures, residual strain in the spiral spring is neglected in the analysis. This assumption will be reexamined in the discussion of the measured resonance frequencies.

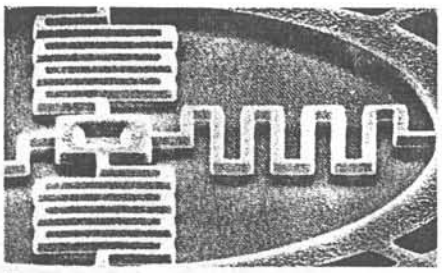

Fig. 3. SEM of one of the four serpentine springs supporting a torsional resonant plate.

The torsional resonance frequency, f_θ, is evaluated by replacing k_{sys} in eqn. (6) by the torsional spring constant, k_θ, and the masses, M_p and M, by the mass moments of inertia, J_p and J:

$$f_\theta = \frac{1}{2\pi}\left[\frac{k_\theta}{(J_p + 0.3714J)}\right]^{1/2} \tag{11}$$

The value of J can be found by evaluating the following integral over the surface area of the plate:

$$J = \int r^2 \, dM = \rho h \int\int r^3 \, d\theta \, dr \tag{12}$$

where ρ is the density of polysilicon (2.3×10^3 kg m^{-3}).

The quality factor is estimated similarly to eqn. (9) by assuming Couette flow underneath the plate, and is given by

$$Q = \frac{d(Jk_\theta)^{1/2}}{\mu \int r^2 \, dA_p} \tag{13}$$

4. Fabrication Process

The structures are fabricated with the four-mask process illustrated in Fig. 4. A significant advantage of this technology is that all the critical features are defined with one mask, eliminating errors due to mask-to-mask misalignment. The process begins with a standard $POCl_3$ blanket n^+ diffusion, which defines the substrate ground plane, after which the wafer is passivated with a layer of 1500 Å-thick LPCVD nitride deposited on top of a layer of 5000 Å-thick thermal SiO_2 (Fig. 4(a)). Contact windows to the substrate ground plane are then opened (Fig. 4(b)) using a combination of plasma and wet etching.

The next steps involve deposition and definition of the first polysilicon layer. A layer of *in situ* phosphorus-doped polysilicon 3000 Å thick is deposited by LPCVD at 650 °C, then patterned with the second mask (Fig. 4(c)). This layer serves as a second electrode plane, the interconnection to

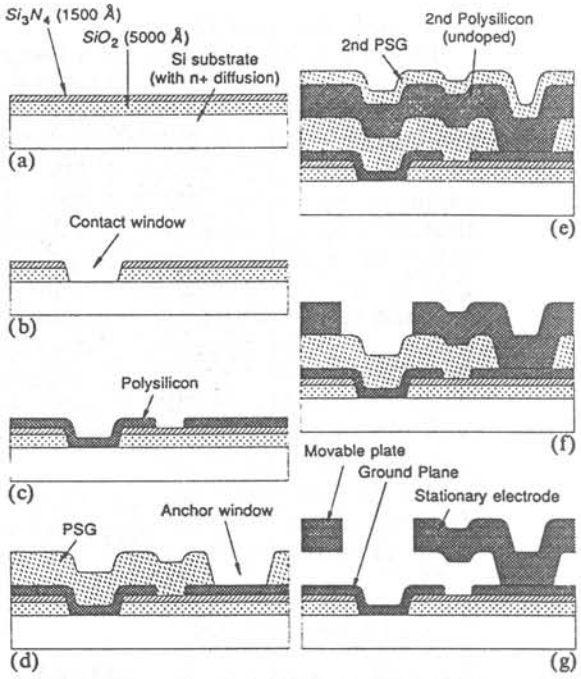

Fig. 4. Process sequence. (a) Deposition of LPCVD nitride on top of a layer of thermal SiO_2. (b) Contact windows to substrate n^+ diffusion. (c) Deposition and patterning of *in situ* P-doped LPCVD polysilicon. (d) Deposition and patterning of sacrificial PSG. (e) Deposition of the undoped LPCVD polysilicon structural layer and a second PSG layer. The wafer is annealed at 950 °C to dope the structural polysilicon layer symmetrically. (f) Patterning of second polysilicon layer. (g) Final cross-section after wet etching of sacrificial PSG.

the n^+ diffusion and for stand-off bumps to prevent sticking of the second polysilicon layer to the substrate after the final micromachining step. (Stand-off bumps are not included in the initial process run.) A 2 μm-thick LPCVD sacrificial phosphosilicate glass (PSG) layer is deposited and patterned with the third mask, as shown in Fig. 4(d), which defines the anchors of the microstructures.

The 2 μm-thick polysilicon structural layer is then deposited by LPCVD (undoped) at 605 °C. The structural layer is doped by depositing another layer of 3000 Å-thick PSG (Fig. 4(e)) and then annealing at 950 °C for one hour. This doping process is designed to dope the polysilicon symmetrically by diffusion from the top and the bottom layers of PSG. A stress-annealing step is then optionally performed at 1050 °C for 30 minutes in N_2. The annealing temperature is lower than 1100 °C in order to avoid loss of adhesion between the PSG and the Si_3N_4 [14, 18].

After stripping the top PSG layer by a timed etch in 10:1 HF, the plates, beams and electrostatic comb drive and sense structures are defined in the final masking step (Fig. 4(f)). The structures are anisotropically patterned in a CCl_4

plasma by reactive-ion etching, in order to achieve nearly vertical sidewalls. Figure 4(g) illustrates the final cross-section after the wafer is immersed in 10:1 diluted HF to etch the sacrificial PSG. The wafer is rinsed repeatedly with DI water for at least 30 minutes after the micromachining step is completed and then dried in a standard spin dryer.

Surface-micromachined polysilicon structures can become stuck to the substrate after the final drying process [20]. The yield of freestanding structures is zero on wafers for which the 30 minute stress anneal at 1050 °C is omitted. When the stress anneal is included in the process, 70% of the structures are freestanding. The 30% that are initially attached to the substrate could be freed easily with a probe tip; the high flexibility of the structures allows them to be manipulated without breakage. No amount of probing, however, could free any of the unannealed structures.

A series of clamped–clamped microbridges is used to estimate the average residual strain in the structural polysilicon film from the minimum buckling length [21]. The moment of the residual strain is studied qualitatively by a series of clamped–free cantilever beams. Since the microbridges have 'step-up' anchors, it is expected that end effects will have to be modeled carefully to obtain an accurate value of the residual strain [22]. Moreover, the 'stiction' of the diagnostic microbridges and cantilevers to the substrate during drying is also a source of error in calculating the strain and its moment [23].

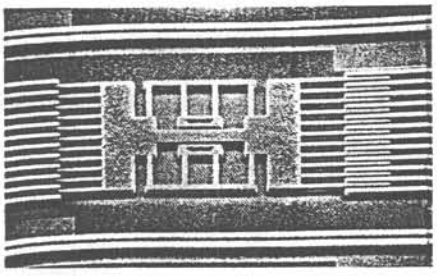

Fig. 5. SEM of a linear resonant plate.

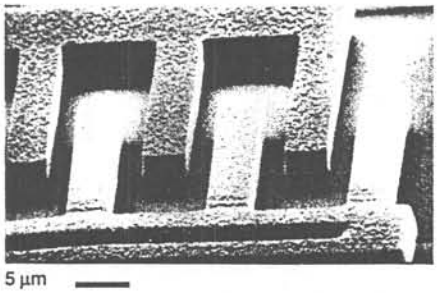

Fig. 6. SEM of a comb structure of the linear resonant plate.

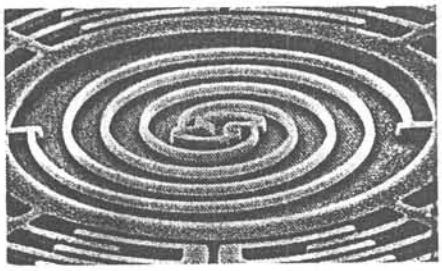

Fig. 7. SEM of two two-turn Archimedean spirals supporting a torsional resonant plate.

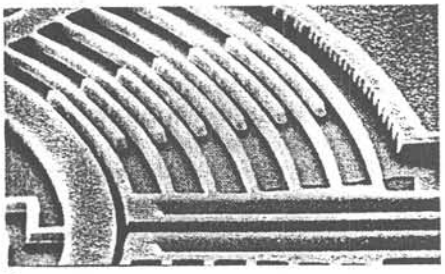

Fig. 8. SEM of a concentric comb-drive structure.

For the unannealed samples, the microcantilevers have a tendency to deflect and attach to the substrate for lengths greater than 150 μm. We interpret the buckling length to be about 120 μm for microbridges using the simple clamped–clamped Euler's criterion [21] and estimate the strain as about 10^{-3}. Annealed samples have apparently undeflected cantilevers under optical and SEM observation and a buckling length of about 220 μm, indicating a residual strain of about 3×10^{-4}. These estimated values are typical of residual strain for phosphorus-doped polysilicon.

Figures 5–8 are scanning-electron micrographs of the completed structures.

5. Experimental Measurements

The resonance frequencies, quality factors and transfer function of the structures with beam lengths of 80 μm or longer can be found by visual observation under 25× magnification. Sinusoidal and d.c. bias voltages are applied to the structures via probes contacting the numbered polysilicon pads in Figs. 1 and 2. For the linear structures, the sinusoidal drive voltage is applied to one set of

fixed electrode fingers via pad 3, while a d.c. bias is supplied to pad 1 (connected to the dormant sense fingers) and pad 2 (connected to the first-level polysilicon ground plane and to the suspended structure). The diffused ground plane is left floating in the initial measurements. The dormant fingers are biased to eliminate electrostatic attraction between them and the resonant structure. For the torsional structures (Fig. 2), the sinusoidal voltage is applied to the drive fingers via pad 2, and the dormant sense fingers, ground plane and resonant structure are biased via pad 1 and pad 3.

In order to provide large-amplitude lateral motion in air for visual observation, d.c. biases of up to 40 V and driving voltage amplitudes (zero to peak) of up to 10 V are used. Resonance frequencies are determined by maximizing the amplitude of vibration, which can be as large as 10 μm for the linear structures with the longest support beams. The measured resonance frequencies for the linear structures are listed in Table 1 and those for the torsional structures are listed in Table 2. The results include measurements from two different electrostatic comb designs (type A and type B), which are described in Table 3 and illustrated in Fig. 9.

TABLE 1. Predicted and measured resonance frequency values of the linear resonant structures

	Type A		Type B	
Beam length (μm)	Predicted (kHz)	Measured (kHz)	Predicted (kHz)	Measured (kHz)
80	75.5	75.0 ± 0.05	71.8	72.3 ± 0.05
100	53.7	54.3 ± 0.05	51.1	50.8 ± 0.05
120	40.6	41.1 ± 0.1	38.7	39.4 ± 0.1
140	32.0	32.0 ± 0.2	30.5	30.0 ± 0.2
160	26.0	25.9 ± 0.2	24.8	25.0 ± 0.2
180	21.7	21.5 ± 0.3	20.7	20.3 ± 0.3
200	18.4	18.2 ± 0.3	17.6	17.5 ± 0.3

TABLE 2. Predicted and measured resonance frequency values of the torsional resonant structures

Supporting beam type	Predicted (kHz)	Measured (kHz)
Spiral	10.5	9.7 ± 0.3
Serpent	60.7	59.4 ± 0.2

TABLE 3. Features of types A and B

Features	A	B
Number of fingers	9	11
Finger width (μm)	4	4
Comb gap (μm)	3	2
Fitted $\partial C/\partial x$ (aF μm^{-1})	58	150

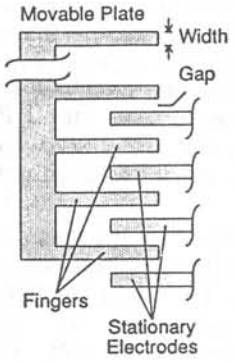

Fig. 9. Comb design parameters.

The calculated resonance frequencies in Tables 1 and 2 are found from eqns. (8) and (9) with the Young's modulus adjusted to give the best fit to the experimental data. For the serpentine-spring torsional structures, a finite-element program [24] is used to find the effective spring constant. The best-fit value for Young's modulus is $E = 140$ GPa for both linear and torsional resonant structures. From Tables 1 and 2, the calculated and measured resonance frequencies are in close agreement for all the lateral structures. It should be noted that, in general, there may be a slight shift in resonance frequencies associated with large-amplitude oscillations [12], although such a shift is not observed with the visual technique employed in the present experiment.

Initial visual measurements of the quality factor Q are plotted in Fig. 10 for the linear resonant structures. The visual measurement of Q is

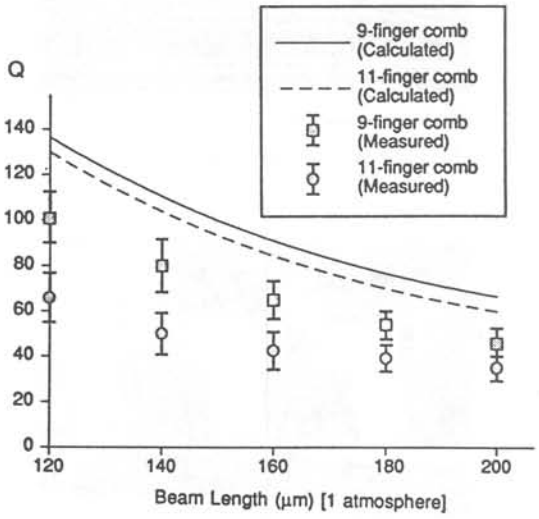

Fig. 10. Plot of measured and calculated values of Q using Couette flow assumption.

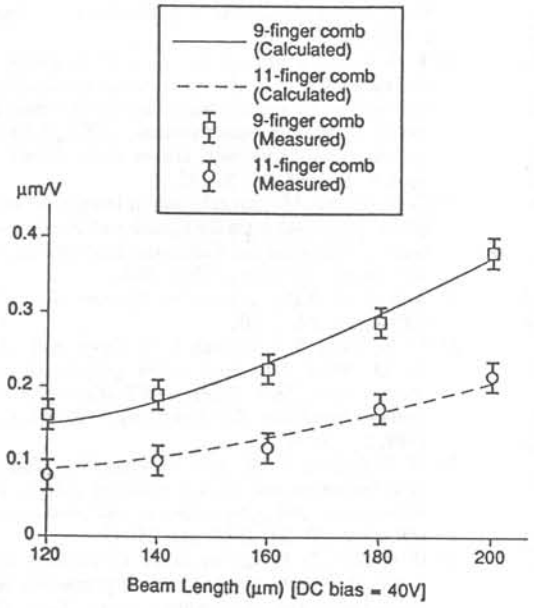

Fig. 11. Measured and calculated values of the transfer functions.

especially difficult for structures with small vibration amplitudes, which is reflected in the larger error bars for these points. The calculated quality factors from eqn. (9) are consistently higher than the measured values, indicating that the assumption of pure Couette flow is an oversimplification for these structures. However, the calculated values of Q are within a factor of two of the actual measurements and may be useful for design purposes. The highest measured Q is about 130 for a structure with 80 μm-long folded-beam suspension.

The magnitude of the electromechanical transfer function is measured by estimating the amplitude of vibration from the envelope of the blurred vibrating structure at a given drive voltage and bias voltage. Figure 11 is a comparison of the experimental results for the linear resonant structures with the calculated values from eqn. (4), for which the capacitance variation ($\partial C/\partial x$) for the two types of comb drives is a fitting parameter. The type A drive is found to have $\partial C/\partial x = 58$ a F μm^{-1} and the type B has $\partial C/\partial x = 150$ a F μm^{-1}.

Electrical characterization of the structures is being pursued. Since buffer circuits are not integrated on-chip along with the resonant structures, the sense current tends to be swamped by feedthrough [14, 18]. The differential drive and sense torsional two-port resonant structure is attractive for minimizing feedthrough.

6. Conclusions

This paper has demonstrated the feasibility and outlined some of the design issues of the electrostatic comb drive and detection of lateral resonant polysilicon microstructures. From the initial visual measurements, it appears that the first-order theory for the transfer function and resonance frequency is adequate for predicting the observed behavior. However, the quality factors calculated from Couette drag due to shear flow beneath the structure consistently overestimate Q. It is likely that the dissipation due to the air movement in the interdigitated fingers is a significant cause of the lower measured quality factors.

The measured resonance frequencies are accurately predicted for all the linear and torsional structures by simple beam theory, using a Young's modulus of 140 GPa and neglecting the residual strain in the released structures. The excellent fit with the measured frequencies over a range of truss dimensions and for the spiral and serpentine springs suggests that the residual strain is effectively relieved in these structures. Otherwise, it would be expected that a shift in frequency from the simple unstrained theory would be observed, with a greater shift for the shorter beams [13]. The value of 140 GPa is less than that measured for fine-grained, undoped polysilicon [13] and greater than that measured for phosphorus-doped, rapid-thermal-annealed polysilicon [25].

An important topic for further research is the simulation and verification of the resonant modes for these complex microstructures [26]. At atmospheric pressure, those modes with motion normal to the substrate are heavily damped, which greatly relaxes the design constraints on the electrostatic comb. For operation in vacuum, design of the drive structure to ensure excitation of a single mode will be challenging, due to the high intrinsic Q of polysilicon microstructures [27].

Acknowledgements

The authors wish to thank D. S. Eddy of General Motors Research Laboratories, Warren, MI, for initial discussions on capacitive excitation, Y.-C. Tai for help with process development, L.-S. Fan for advice on polysilicon properties, S. Hoagland, and R. M. Hamilton, M. Kushner, and K. Voros of the UC Berkeley Microfabrication Facility for invaluable assistance in processing the devices. This project is funded by General Motors Research Laboratories, Warren, MI, through the Berkeley Sensor & Actuator Center.

References

1 R. T. Howe, Resonant microsensors, *Tech. Digest, 4th Int. Conf. Solid-State Sensors and Actuators (Transducers '87), Tokyo, Japan, June 2–5, 1987*, pp. 843–848.

2 M. A. Schmidt and R. T. Howe, Resonant structures for integrated sensors, *Tech. Digest, IEEE Solid-State Sensor Workshop, Hilton Head Island, SC, U.S.A., June 2–5,* 1986, pp. 94–97.

3 R. M. Langdon, Resonator sensors—a review, *J. Phys. E: Sci. Instrum, 18* (1985) 103–115.

4 E. P. EerNisse and J. M. Paros, Practical considerations for miniature quartz resonator force transducers, *Proc. 37th Ann. Symp. Freq. Control, Philadelphia, PA, U.S.A.*, pp. 255–260.

5 J. G. Smits, H. A. C. Tilmans and T. S. J. Lammerink, Pressure dependence of resonant diaphragm pressure sensors, *Tech. Digest, 3rd Int. Conf. Solid-State Sensors and Actuators (Transducers '85), Philadelphia, PA, U.S.A., June 11–14, 1985,* pp. 93–96.

6 J. C. Greenwood, Etched silicon vibration sensor, *J. Phys. E: Sci. Instrum., 17* (1984) 650–652.

7 K. Ikeda, H. Kuwayama, T. Kobayashi, T. Watanabe, T. Nishikawa and T. Yoshida, Silicon pressure sensor with resonant strain gauges built into diaphragm, *Tech. Digest, 7th Sensor Symp., Tokyo, Japan, May 30–31, 1988,* pp. 55–58.

8 D. C. Satchell and J. C. Greenwood, Silicon microengineering for accelerometers, *Proc. Inst. Mech. Eng., 1987–2, Mechanical Technology of Inertial Devices, Newcastle upon Tyne, U.K., Apr. 7–9, 1987,* pp. 191–193.

9 R. T. Howe and R. S. Muller, Resonant-microbridge vapor sensor, *IEEE Trans. Electron Devices, ED-33* (1986) 499–506.

10 W. Benecke, A. Heuberger, W. Reithmüller, U. Schnakenberg, H. Wölfelschneider, R. Kist, G. Knoll, S. Ramakrishnan and H. Höfflin, Optically excited mechanical vibrations in micromachined silicon cantilever structures, *Tech. Digest, 4th Int. Conf. Solid-State Sensors and Actuators (Transducers '87), Tokyo, Japan, June 2–5, 1987,* pp. 838–842.

11 H. C. Nathanson, W. E. Newell, R. A. Wickstrom and J. R. Davis, Jr., The resonant gate transistor, *IEEE Trans. Electron Devices, ED-14* (1987) 117–133.

12 K. E. Petersen and C. R. Guarnieri, Young's modulus measurements of thin films using micromechanics, *J. Appl. Phys., 50* (1979) 6761–6766.

13 D. W. DeRoo, Determination of Young's modulus of polysilicon using resonant micromechanical beams, *M.S. Rep.*, Department of Electrical and Computer Engineering, University of Wisconsin—Madison, Jan. 1988.

14 M. W. Putty, Polysilicon resonant microstructures, *M.S. Thesis*, Department of Electrical Engineering and Computer Science, The University of Michigan, Ann Arbor, MI., Sept. 1988.

15 M. A. Schmidt, Microsensors for the measurement of shear forces in turbulent boundary layers, *Ph.D. Thesis*, Massachusetts Institute of Technology, Cambridge, MA., May 1988.

16 M. A. Schmidt, R. T. Howe, S. D. Senturia and J. H. Haritonidis, Design and calibration of a microfabricated floating-element shear-stress sensor, *IEEE Trans. Electron Devices, ED-35* (1988) 750–757.

17 A. P. Pisano, Resonant-structure micromotors, *Tech. Digest, IEEE Micro Electro Mechanical Systems Workshop, Salt Lake City, UT, U.S.A., Feb. 20–22, 1989,* pp. 44–48.

18 R. T. Howe, Integrated silicon electomechanical vapor sensor, *Ph.D. Thesis*, Department of Electrical Engineering and Computer Sciences, University of California at Berkeley, Dec. 1984.

19 A. M. Wahl, *Mechanical Springs*, Penton, Cleveland, 1st edn, 1945.

20 T. A. Lober and R. T. Howe, Surface-micromaching processes for electrostatic microactuator fabrication, *Tech. Digest, IEEE Solid-State Sensor and Actuator Workshop, Hilton Head Island, SC, U.S.A., June 6–9,* 1988, pp. 59–62.

21 H. Guckel, T. Randazzo and D. W. Burns, A simple technique for the determination of mechanical strain in thin films with applications to polysilicon, *J. Appl. Phys., 57* (1985) 1671–1675.

22 T. A. Lober, J. Huang, M. A. Schmidt and S. D. Senturia, Characterization of the mechanisms producing the bending moments in polysilicon microcantilever beams by interferometric deflection measurements, *IEEE Solid-State Sensor and Actuator Workshop, Hilton Head Island, SC, U.S.A., June 6–9, 1988,* pp. 92–95.

23 D. W. Burns, Micromechanics of integrated sensors and the planar processed pressure transducer, *Ph.D. Thesis*, Department of Electrical and Computer Engineering, University of Wisconsin—Madison, May 1988.

24 *SuperSAP*, Algor Interactive Systems, Inc., Essex House, Pittsburgh, PA 15206.

25 M. W. Putty, S.-C. Chang, R. T. Howe, A. L. Robinson and K. D. Wise, One-port active polysilicon resonant microstructures, *Tech. Digest, IEEE Micro Electro Mechanical Systems Workshop, Salt Lake City, UT, U.S.A., Feb. 20–22,* 1989, pp. 60–65.

26 M. V. Andres, K. W. H. Foulds and M. J. Tudor, Sensitivity of a frequency-out silicon pressure sensor, *Tech. Digest, Eurosensors, 3rd Symp. Sensors and Actuators, Cambridge, UK, Sept. 22–24,* 1987, *pp. 18–19.*

27 H. Guckel, D. W. Burns, H. A. C. Tilmans, D. W. DeRoo and C. R. Rutigliano, Mechanical properties of fine grained polysilicon—the repeatability issue, *Tech. Digest, IEEE Solid-State Sensor and Actuator Workshop, Hilton Head Island, SC, U.S.A., June 6–9,* 1988, pp. 96–99.

Biographies

William. C. Tang received the M.S. degree in electrical engineering from the University of California at Berkeley in 1982. He has been an associate engineer/scientist at IBM Corp., San Jose, California since 1982. In 1984, he returned to U.C. Berkeley to pursue a Ph.D. degree in electrical engineering. His field of study is in micromachined electromechanical systems. Mr Tang is a student member of the IEEE and Eta Kappa Nu.

Tu-Cuong (Clark) Nguyen received the B.S. degree in electrical engineering and computer sciences from the University of California at Berkeley in 1988. He is presently enrolled in an M.S./Ph.D. program with the Department of Electrical Engineering and Computer Sciences at U.C. Berkeley.

Roger T. Howe received the Ph.D. degree in electrical engineering from the University of California at Berkeley in 1984. He was on the faculty of Carnegie–Mellon University during 1984–1985 and was an assistant professor at the Massachusetts Institute of Technology from 1985 to 1987. In 1987, he joined the Department of Electrical Engineering and Computer Sciences at the University of California at Berkeley, where he is now an associate professor and an associate director of the Berkeley Sensor & Actuator Center. His research interests include resonant microsensors and microactuators, micromachining technology and integrated-circuit design. Dr Howe is a member of the IEEE, the Materials Research Society, the Electrochemical Society and Sigma Xi.